Onset and breakdown of relaxation oscillations in the torsional Quincke pendulum

Michael A. Zaks
Humboldt University of Berlin, D-12489 Berlin, Germany

Mark I. Shliomis
Ben-Gurion University, Beer-Sheva 84105, Israel

In a strong constant electric field, a dielectric particle immersed in a weakly conducting fluid exhibits spontaneous rotations. This phenomenon is known under the name of the Quincke effect. In the original setup the particle was suspended on a silk thread and performed torsional oscillations of remarkably high amplitude. We derive the governing equations for this experiment, and ascertain that onset of oscillations from the quiescent state corresponds to the supercritical Hopf bifurcation. For the case of a soft thread, we characterize the regime of large-scale torsional relaxation oscillations: explicit estimates are derived for their period and amplitude, effects of bifurcation delay are described. In a stronger electric field, these relaxation oscillations yield to small-scale erratic rotations of the pendulum.

PACS numbers: 45.20.dc, 47.65.-d, 02.30.Oz

I. INTRODUCTION

In the last decade of the 19th century Georg Quincke performed and meticulously described experiments in which various dielectric objects were suspended on thin threads and put between the vertical plates of capacitor filled with weakly conducting liquid. As soon as the strong constant electric field was switched on, the objects started to rotate clockwise or counterclockwise around the suspension axis [1]. To enable rotations, the field strength had to exceed a certain threshold value which depended on the properties of the experimental setup. Quincke measured amplitudes and periods of torsional oscillations for different field strengths, different liquids, different sorts of dielectrics and different shapes (rods, spheres, cylinders) and sizes of objects. Remarkably, in strong fields the registered amplitude of oscillation was quite large: between the reversal points, hundreds of revolutions of suspended bodies were counted (cf. Tables in p. 435 of [1]).

Nowadays, spontaneous rotation of dielectric particles in the constant electric field is known as the Quincke effect. Quincke himself ascribed it to the action of the thin film of air between the body and the fluid: displacement of electric flux lines, caused by the difference of permittivities, deforms the film and creates the pressure gradient which, in its turn, generates the torque responsible for the rotation. A more accurate quantitative description was obtained in the second half of the 20th century: it was shown, that the torque originated in the difference between the relaxation times for electric charges in the liquid and in the solid body [2, 3].

In recent years, Quincke effect was found to stay behind non-trivial collective phenomena in suspensions of dielectric particles in weakly conducting fluids. Onset of Quincke rotation has been demonstrated to decrease the effective viscosity of such suspensions [4]. Furthermore, the Quincke rotation of insulating grains facilitates the convective transfer of the electric charge through the liquid. Thereby – somewhat counter-intuitively – adding nonconducting particles to the suspension is able to increase its bulk conductivity [5].

In absence of the thread, equations which govern dynamics of a solitary insulating particle immersed in a weakly conducting fluid and exposed to a constant electric field, have been found to be equivalent to the well-known Lorenz equations [6], a prototype of deterministic aperiodic dynamics; subsequent experiments have confirmed existence of stationary and chaotic rotations [8].

Here, we return to the original experimental setup and consider the case of a solid body suspended on an elastic thread. We derive a set of governing equations for the body, and demonstrate that transition to torsional oscillations occurs through the supercritical Hopf bifurcation.

In his account, Georg Quincke noted that "immediately after the reversal, the fast turns follow, which gradually slow down, terminate and change the direction" (p. 429 of [1]); "in viscous fluids the angular velocity is independent of the torsional angle of the thread, and stays constant for the long time" (*ibid.*, p.431). This description implies that the observed torsional oscillations were strongly anharmonic; in the modern parlance they would be probably referred to as relaxation oscillations. In his experiments, Quincke used silk threads because he "had found no other substance which would withstand without rupture such a big number of revolutions as silk" (p. 430 of [1]). In accordance with this, we mostly concentrate on the case of "soft" suspension, where the problem possesses two disparate timescales: the slow mechanical timescale and the fast electric one.

Separation of timescales permits to characterize explicitly the regime of relaxation oscillations, providing estimates for their amplitude and period. Since the subspace corresponding to the fast dynamics is three-dimensional, both the approach to and the departure from the slow regime may be monotonic or oscillatory; we describe the corresponding effects and their implications. In partic-

ular, the oscillatory departure from the slow state is a consequence of the subcritical Hopf bifurcation in the fast system; therefore, the observable period of torsional oscillations is not an intrinsic characteristics of the system but sensitively depends on the level of noise in the experiment or on the precision of calculations in the case of numerical simulation.

The layout of the paper is as follows. In the next section we describe the physical object and derive the equations which govern its dynamics. Section III contains the results of weakly nonlinear analysis close to the stability threshold of the quiescent state. It turns out that for soft suspension threads, the domain of applicability of weakly nonlinear predictions is strongly restricted. To explain this effect, we perform in Sect. IV separation of timescales and evaluate the period and the amplitude of the relaxation torsional oscillations. In Sect. V the phenomenon of bifurcation delay is treated: we discuss the relationship between the observed characteristics of oscillations and the level of numerical inaccuracies or fluctuations in an experimental setup.

II. SETUP AND GOVERNING EQUATIONS

Consider an axially symmetric dielectric solid object suspended inside the weakly conducting fluid on an elastic thread. Fig. 1 shows two exemplary configurations and a convenient reference frame which we use hereafter: x-axis is directed along the constant horizontal electrical field $\boldsymbol{E}$, and z-axis, respectively, upwards along the thread.

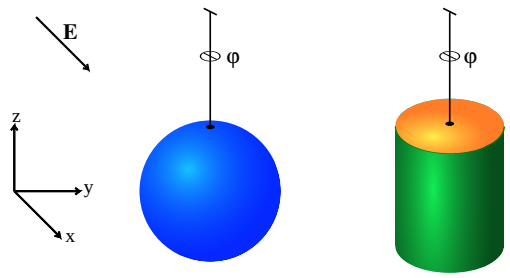

FIG. 1: (color online) Axially symmetric dielectric bodies suspended in the weakly conducting fluid. Direction of x-axis is parallel to the horizontal permanent electric field $\boldsymbol{E}$.

In the derivation of equations of motion for the resulting torsional pendulum we follow the spirit and, partially, notation of [2, 6] where the similar situation (but without a thread) was considered. Interaction of the total dipole moment of the suspended body $\boldsymbol{P}_{\rm tot}$ with the external constant field $\boldsymbol{E}$ generates a torque which acts upon the body. This torque is counteracted by elasticity of the thread as well as by viscous friction between the body and the surrounding fluid. Let the elastic force obey Hooke's law; in case, say, of a silk thread, the latter holds for quite sizeable deflections.

The viscous torque deserves a more elaborate discussion. We restrict our analysis to the Stokes approximation, so that the nonlinear terms in the Navier-Stokes equations can be disregarded. This requires smallness of the Reynolds number. Within the Stokes equation, the axial symmetry of the problem admits (in general, time-dependent) axisymmetric flow patterns in which both the radial and the axial components of velocity are absent, and the remaining azimuthal component v_φ is φ-independent.

Let the instantaneous angular velocity of the body be $\boldsymbol{\Omega}=(0,0,d\varphi/dt)$. The overall instantaneous viscous torque with which the axisymmetric flow pattern acts upon this body equals

$$M \;=\; -2\pi\eta \int (1+\mathcal{R}'^2(z))\;(r^2\frac{\partial v_\varphi}{\partial r} - r\,v_\varphi\,)\Big|_{r=\mathcal{R}(z)} dz$$

where η is the dynamical viscosity of the fluid, r denotes the radial coordinate, $\mathcal{R}(z)$ is the value of r at the lateral boundary of the body, and integration is performed along the axial direction.

The Reynolds number of the flow $Re=\Omega\mathcal{R}^2/\nu$ can be viewed as the ratio of the characteristic "viscous" time $\mathcal{R}^2/\nu$ and the "rotational" time $1/\Omega$. Since the Stokes approximation is based on the assumption $Re \ll 1$, the typical lifetime of viscous perturbations is much smaller than the typical duration of one revolution of the body. In other words, changes in the angular velocity of the rotating body are accompanied by nearly instantaneous relaxation of the velocity field in the bulk of the fluid. This allows us in our treatment below to neglect corrections caused by non-stationarity (cf. §24 of [7]) and to use for the frictional torque the values, produced by stationary velocity fields. As a consequence, the torque becomes proportional to the angular velocity of the body.

Balance of torques governs dynamics of the deflection angle φ of the pendulum:

$$I\,\frac{d^2\varphi}{dt} \;=\; (\boldsymbol{P}_{\rm tot}\times\boldsymbol{E})_z \;-\alpha\,\frac{d\varphi}{dt} - \beta\,\varphi\,. \qquad (1)$$

Here, I is the moment of inertia of the body, α is the coefficient of the torsional viscous friction and, finally, β is the torsional elastic coefficient of the suspension thread.

The total dipole moment $\boldsymbol{P}_{\rm tot}$ consists of two parts: $\boldsymbol{P}_{\rm tot}=\boldsymbol{P}_\infty+\boldsymbol{P}(t)$. Instantaneous polarization $\boldsymbol{P}_\infty=\chi_\infty\boldsymbol{E}$ is proportional to the applied constant field; here χ_∞ is the high frequency dielectric susceptibility. The time-dependent component $\boldsymbol{P}(t)$ is the retarding polarization caused by accumulation of free charges on the liquid-solid boundary.

Two factors are responsible for evolution of $\boldsymbol{P}(t)$: relaxation of the dipole magnitude and direction, as well as variation of the direction caused by the body rotation. Accordingly, the evolution equation contains two

terms [2]:

$$\frac{d\boldsymbol{P}}{dt} = -\frac{\boldsymbol{P}_{\rm tot} - \chi_0 \boldsymbol{E}}{\tau_M} + \boldsymbol{\Omega} \times \boldsymbol{P} \qquad (2)$$

In terms of the angle φ and horizontal components of polarization P_x and P_y, equations (1) and (2) yield

$$\begin{aligned} I\,\frac{d^2\varphi}{dt} &= -P_y\,E - \alpha\frac{d\varphi}{dt} - \beta\varphi \\ \frac{d\,P_x}{dt} &= -P_y\frac{d\varphi}{dt} - \frac{P_x}{\tau} + \frac{E(\chi_0 - \chi_\infty)}{\tau} \\ \frac{d\,P_y}{dt} &= P_x\frac{d\varphi}{dt} - \frac{P_y}{\tau} \end{aligned} \qquad (3)$$

Dynamics in the system (3) depends, of course, on the values of the coefficients in these equations. Of these only one characterizes the thread: for a filament with length h and diameter d, the coefficient of torsional elasticity β equals $\pi d^4 G/(32h)$ where G denotes the rigidity modulus of the filament stuff. The rest: moment of inertia I, the coefficient of torsional viscous friction α, the values of the instantaneous susceptibility χ_∞, static susceptibility χ_0 and the Maxwell relaxation time τ are related to the shape and size of the body. The last three coefficients depend also on the electric characteristics of the setup: permittivities $\varepsilon_{l,s}$ and conductivities $\gamma_{l,s}$ (here and below, indices l and s refer, respectively, to the liquid and the solid media). Below, we quote these coefficients for simple configurations from Fig. 1.

For a sphere of mass m and radius a, one has $I = 2ma^2/5$, $\alpha = 8\pi\eta a^3$, Maxwell relaxation time is $\tau = (2\varepsilon_l + \varepsilon_s)/(2\gamma_l + \gamma_s)$, and susceptibilities are given by $\chi_\infty = a^3\varepsilon_l\,(\varepsilon_s - \varepsilon_l)/(2\varepsilon_l + \varepsilon_s)$ and $\chi_0 = a^3\varepsilon_l(\gamma_s - \gamma_l)/(2\gamma_l + \gamma_s)$.

For a sufficiently long cylinder with mass m, radius a and height L, the respective values are: $I = ma^2/2$, $\alpha = 4\pi\eta a^2 L$, $\tau = (\varepsilon_l+\varepsilon_s)/(\gamma_l+\gamma_s)$, $\chi_\infty = 2\pi a^2 L\varepsilon_l(\varepsilon_s - \varepsilon_l)/(\varepsilon_s + \varepsilon_l)$ and $\chi_0 = 2\pi a^2 L\varepsilon_l(\gamma_s - \gamma_l)/(\gamma_s + \gamma_l)$.

It is convenient to measure time in units of τ. In terms of the (reversed) angular velocity $X = -\dot\varphi$ and dimensionless variables

$$Y = \frac{P_y E\tau}{\alpha}, \qquad Z = \frac{\big(P_x - (\chi_0 - \chi_\infty)E\big)\,E\,\tau}{\alpha},$$

equations (3) turn into the "Lorenz-like" form

$$\begin{aligned} \dot X &= \sigma(Y - X) + \nu^2\varphi, \\ \dot Y &= X\,(R - Z) - Y, \\ \dot Z &= X\,Y - Z, \\ \dot\varphi &= -X, \end{aligned} \qquad (4)$$

where the dot denotes differentiation with respect to dimensionless time t/τ, the new parameters σ and R are defined as

$$\sigma = \frac{\alpha\tau}{I}, \qquad R = \frac{(\chi_\infty - \chi_0)E^2\tau}{\alpha},$$

and, finally, $\nu = \tau\sqrt{\beta/I}$ is the dimensionless eigenfrequency of the torsional pendulum.

Let us briefly discuss the parameters and general properties of the system (4). Of the variables, the deflection angle φ is directly amenable to experimental measurements, whereas dynamics of re-scaled dipole components Y and Z is much more difficult to resolve. Of the three participating parameters σ, ν and R the former two are non-negative. The parameter σ is proportional to coefficient of viscous friction α and characterizes the dissipation. Recent experimental measurements on Quincke rotation of glass tubes in transformer oil correspond, in these terms, to σ=14.6 [6] and σ=2.5 [8]. The values of eigenfrequency ν are larger for thick short stiff threads, and can be decreased by choosing longer, thinner and/or softer threads. The parameter R, proportional to the square of the field strength E, characterizes the external pumping. Depending on the sign of $\chi_\infty - \chi_0$, R can be of either sign. As we will see below, non-steady dynamics in equations (4) can occur only at positive values of R. This imposes a condition for susceptibilities: $\chi_\infty > \chi_0$, which, in terms of the media characteristics, implies $\varepsilon_s/\varepsilon_l > \gamma_s/\gamma_l$. If this inequality is fulfilled, the dipole moment of the body, induced by the field $\boldsymbol{E}$, is directed opposite to this field, and the potentially unstable situation arises [9].

Equations (4) are invariant with respect to simultaneous change of sign of φ, X and Y; this reflects the obvious symmetry between the clockwise and counterclockwise rotation directions. At $\nu = 0$ the last equation decouples, and the first three ones turn into the famous Lorenz equations, a prototype of deterministic chaos [17]. Thereby the angle φ becomes, up to a sign, an integral of the chaotic variable $X(t)$ over time. Equivalence between the Lorenz equations and the equations of a free rotating dielectric body in the constant electric field was established in [6]; in the subsequent publication [8], this conclusion was confirmed through accurate experimental comparison.

III. LINEAR AND WEAKLY NONLINEAR ANALYSIS

Under all parameter values, equations (4) possess a unique steady solution $\varphi = \dot\varphi = Y = Z = 0$ which corresponds to the quiescent state without torsional deformation of the thread. As long as the applied electric field is sufficiently weak, this equilibrium is asymptotically stable; increase of the field intensity (manifested in the growth of the parameter R) eventually results in its destabilization. Onset of oscillations with the critical frequency ω_c follows the Andronov-Hopf bifurcation at the threshold value $R = R_c$:

$$R_c = 1 + \frac{\nu^2}{1+\sigma}, \qquad \omega_c = \frac{\nu}{\sqrt{1+\sigma}}. \qquad (5)$$

Notably, $\omega_c < \nu$. Expansion of the oscillation amplitude up to the cubic terms yields asymptotic parameter dependencies for the maximal deflection angle $\varphi_{\max}$ and frequency of oscillations ω:

$$\varphi_{\max}(R) = \frac{2(1+\sigma)}{\nu}\sqrt{\frac{(1+\sigma+4\nu^2)(R-R_c)}{3[(1+\sigma)^2+(1+2\sigma)\nu^2]}} + O(R-R_c) \quad (6)$$

and

$$\omega(R) = \omega_c\left[1+\frac{\sigma(1+\sigma)(R-R_c)}{2[(1+\sigma)^2+(1+2\sigma)\nu^2]}\right] + O\big[(R-R_c)^2\big]. \quad (7)$$

Since the coefficient at $(R-R_c)$ in Eq. (6) is positive for all positive values of σ and ν, the bifurcation is invariably supercritical. This fact has important physical implications: variations of mechanical (shape, size, density and material of the body, length and material of the thread, viscosity of the fluid etc.) and electrical (permittivities and conductivities) characteristics of the setup, change, of course, the threshold value for the field intensity and the frequency of oscillations at their onset. Irrespectively of this, however, transition from quiescent state to oscillations is always of the soft type, and the amplitude of the newborn oscillations is small. The above assumptions of the Hooke torsional elasticity and moderate Reynolds number are irrelevant for this conclusion as well: although they may get questionable for fast large-scale oscillations, sufficiently close to the equilibrium both the deflections and the angular velocities are small enough to ensure linearity. Noteworthy, Eq. (7) predicts monotonic growth of the oscillation frequency with the increase of R.

Estimates (6) and (7) are asymptotically correct for $R \to R_c$; let us test their accuracy numerically at finite distances from the threshold. Fig. 2 indicates that for sufficiently stiff threads both estimates overshoot the actual values but remain reasonably accurate even at $R - R_c \approx 1$.

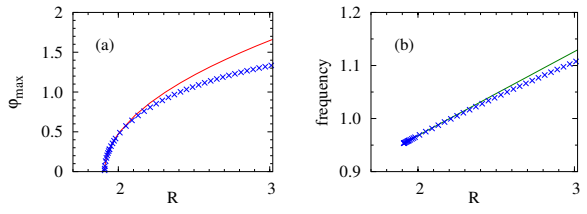

FIG. 2: (color online) Amplitude and frequency of oscillations at $\sigma = 10$, $\nu^2 = 10$. $R_c = 1.909$, $\omega_c = 0.953$. Solid lines: estimates (6,7). Crosses: numerically obtained values.

However, for soft threads with small values of ν^2 the picture looks quite different. As seen in the top panels of Fig. 3, at low values of ν the working range of R for

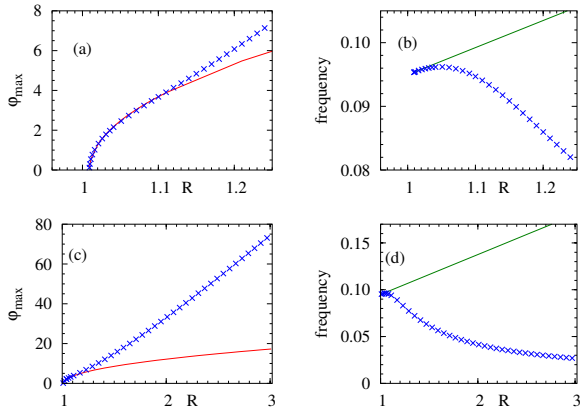

FIG. 3: (color online) Amplitude and frequency of oscillations at $\sigma = 10$, $\nu^2 = 0.1$. $R_c = 1.00909$, $\omega_c = 0.0953$. Solid lines: estimates (6,7). Crosses: numerical values.

the estimates (6,7) is pretty small. Close to the threshold, the mismatch for the estimate of the amplitude (left top panel) is not indeed dramatic. For the frequency of oscillations, however, the discrepancy is qualitative: the actual values of the frequency, after an initial very short range of growth, start to decay. Computations further from the threshold, visualized in the bottom panels of Fig. 3, show the growth of mismatch: at $R - R_c \approx 2$ the predicted value of the amplitude is 4 times smaller than the actual one, whereas the frequency attains values which are almost 7 times smaller than the predictions and 4 times lower than critical frequency at the onset of oscillations. Compared to the weakly nonlinear estimates, torsional oscillations become rather large and acquire long periods.

IV. PENDULUM ON A SOFT THREAD: SEPARATION OF TIMESCALES AND ESTIMATES OF CHARACTERISTICS

From now on, we concentrate on the case of soft thread, $\nu^2 \ll 1$. To begin with, let us briefly recall the case of "pure" Lorenz dynamics at $\nu = 0$. For $R < 1$ the trivial equilibrium $X = Y = Z = 0$ is the unique attractor. For $R > 1$, two symmetric stationary solutions exist: $X = Y = \pm\sqrt{R-1}$, $Z = R$–1. These fixed points are stable for arbitrary R if $\sigma < 2$, otherwise they are stable for $R < R_h = \sigma(\sigma+4)/(\sigma-2)$. At $R = R_h$ the subcritical (hard mode) Hopf bifurcation takes place. In a large range of R beyond R_h the dynamics is chaotic. In fact, the skeleton of the chaotic set emerges in the phase space already well below R_h at the so-called homoclinic explosion [11]. The newborn chaotic set is repelling, but when R is increased, it acquires attracting properties and coexists with stable equilibria in a certain range of R.

A. Curve of slow motions: general aspects

From the point of view of pendulum, nontrivial stationary solutions of the Lorenz equations are regimes of rotation with constant angular velocity $-X$: $\varphi(t) = \varphi(0) - X\,t$. In the phase space, fixed points of the Lorenz equations turn into invariant straight lines upon which the values of φ are unbounded.

Introduction of torsional elasticity disables unbounded rotations. In order to follow the breakup of straight lines, let us rescale the angle variable: $\varphi = -\Psi\sigma/\nu^2$. In terms of Ψ, equations (4) become

$$\begin{aligned} \dot{X} &= \sigma(Y - X - \Psi), \\ \dot{Y} &= X\,(R - Z) - Y, \\ \dot{Z} &= X\,Y - Z, \\ \dot{\Psi} &= \epsilon X \end{aligned} \qquad (8)$$

with the small parameter $\epsilon \equiv \nu^2/\sigma$. Note that $|\Psi|$ is not necessarily small, since the initial variable φ in the non-perturbed case can assume arbitrarily large values.

The system (8) displays the obvious separation of timescales: dynamics of X, Y and Z is "fast" whereas the variable Ψ, according to the last equation, is slow. For sufficiently small values of ϵ, Ψ turns into a "frozen" inhomogeneity in the first equation. On the fast timescale t, one observes dynamics of the asymmetric Lorenz equations with parameters σ and R, and pseudo-parameter Ψ. On the slow timescale ϵt, the evolution of Ψ obeys $d\Psi/d(\epsilon t) = \langle X \rangle$ where averaging is performed over the fast time.

Behavior in the full system of equations corresponds to the drift across the parameter space of the asymmetric Lorenz equations. Depending on the value of R and instantaneous value of Ψ, it is a motion through the domains of stationary or chaotic dynamics in the fast subsystem. In the former case, when attractor of the fast equations is a fixed point, explicit characteristics of dynamics can be obtained in the closed form. Solving for steady solutions of the first three equations in (8) as functions of R and Ψ, we find $Y = X + \Psi$, $Z = X(X + \Psi)$ where X is a root of the cubic equation

$$X^3 + X^2\Psi + X\,(1 - R) + \Psi = 0. \qquad (9)$$

With Ψ running through all real values, the set of these points forms a one-dimensional curve of slow motions (referred below as "slow curve") in the four-dimensional phase space of the full problem. The slow equation $\dot{\Psi} = \epsilon X$ lets Ψ increase (on the slow timescale) if the value of X is positive and decrease otherwise.

It is convenient to parameterize the slow curve not by Ψ, but by X; for this purpose Eq. (9) is inverted, yielding a dependence of Ψ on the "stationary" value of X:

$$\Psi(X) = \frac{R\,X}{1 + X^2} - X. \qquad (10)$$

Slow evolution of X *along* the slow curve is governed by

$$\dot{X} = -\epsilon\,\frac{X\,(1 + X^2)^2}{(1 + X^2)^2 - R(1 - X^2)} \qquad (11)$$

Typical shapes of the slow curve are plotted in Fig.4. For $R \le 1$ (left panel) the function $\Psi(X)$ is monotonically decreasing, and the denominator in Eq.(11) is positive. Accordingly, on the slow timescale the motions decay to the trivial equilibrium $X = Y = Z = \Psi = 0$. For $R > 1$ (right panel) the dependence $\Psi(X)$ is N-shaped: the right and the left branches of the curve are decreasing whereas on the middle segment the function is increasing. The local maximum lies at

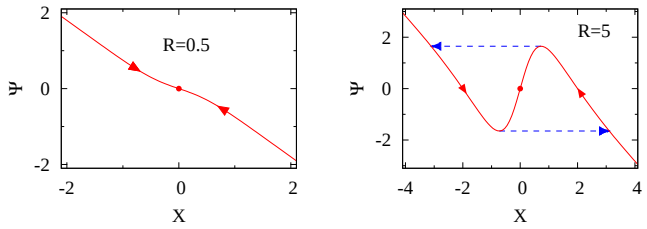

FIG. 4: (color online) Dependence $\Psi(X)$ on the slow curve. Arrows: directions of motion. Dashed lines: fast "jumps".

$$X_m = \left(\frac{\sqrt{R^2 + 8R} - R - 2}{2}\right)^{1/2}$$

and equals

$$\Psi_m = \left(\frac{R^2 - 20R - 8 + \sqrt{R(8 + R)^3}}{8}\right)^{1/2};$$

the local minimum at $X = -X_m$ equals $-\Psi_m$.

To check whether the slow curve is attracting, we linearize the fast equations near a point with coordinate X_0 upon this curve, and obtain the characteristic polynomial

$$\begin{aligned} \lambda^3 &+ \lambda^2(\sigma + 2) + \lambda\left(1 + 2\sigma + X_0^2 - \frac{\sigma R}{1 + X_0^2}\right) \\ &+ \sigma\left(X_0^2 + R + 1 - \frac{2R}{1 + X_0^2}\right) = 0 \end{aligned} \qquad (12)$$

Passage through $\pm X_m$ corresponds to the saddle-node bifurcation in the fast system: two equilibria appear/die. At $X_0 = \pm X_m$, Eq.(12) possesses a zero root.

For the whole middle segment $-X_m < X_0 < X_m$, the last term in (12) is negative at $R > 1$, hence at least one of the eigenvalues λ is real and positive. Accordingly, the middle segment is repelling; its points are saddle points of the fast system. Stability of the outer segments depends on the values of R and σ.

Both side branches of the slow curve are locally stable as a whole, provided the inequality

$$R < R_{\rm TB} = \frac{4 + 3\sigma^2 - (\sigma - 2)\sqrt{4 + 4\sigma + 9\sigma^2}}{2\sigma} \qquad (13)$$

holds. In this situation a node which participates in the saddle-node bifurcation of the fast system $\Psi = \pm\Psi_m$ is a *stable* node. For $R > R_{\rm TB}$ this node is unstable, and the adjoining segment of the side branch is unstable. At $R = R_{\rm TB}$ and $X_0 = \pm X_m$ Eq.(12) has two zero solutions: this is the codimension-2 Takens-Bogdanov bifurcation in the fast system.

Let us follow the dynamics of the system at $1 < R < R_{\rm TB}$. Taken initial conditions somewhere on the right branch, the imaging point slowly – with the velocity (11) – climbs this branch upwards, until reaching the maximum Ψ_m at X_m. Since the value of X at this critical point is positive, Ψ should grow further. Therefore, the imaging point is forced to detach from the slow curve, and a rapid evolution on the fast timescale sets on. During the fast motion the value of Ψ remains almost frozen a bit above Ψ_m, whilst X finally settles on the left branch at

$$X_s = -\left(\frac{(\sqrt{R^2+8R}+R)^2}{16} - 1\right)^{1/2} :$$

for $\Psi > \Psi_m$ the equilibrium on the left branch is the sole attractor of the fast system. This flight is followed by another interval of slow motion: since on the left branch the angular velocity is negative, the system moves downwards. On reaching the minimum, it jumps back to the right branch, and completes thereby the cycle which consists of creeping motions along two slow segments separated by two swift jumps. In Fig. 4 the jump stages are indicated by dashed arrows. In fact, this is the classical textbook mechanism which ensures, for example, the onset of relaxation oscillations in the Van der Pol equation [18].

B. Estimates of amplitude and period

Variable Ψ oscillates between $-\Psi_m$ and Ψ_m. Accordingly, the original angle variable φ of (3) and (4) exhibits periodic relaxational oscillations with the amplitude $\Phi_0 = 2\sigma\Psi_m/\nu^2$, or, in terms of R,

$$\Phi_0 = \frac{\sigma}{\nu^2}\left(\frac{R^2 - 20R - 8 + \sqrt{R(8+R)^3}}{2}\right)^{1/2}. \qquad (14)$$

When estimating the period of those oscillations, we neglect the duration of fast jumps; integration of (11) along the relevant segments of the slow curve renders expression for the period

$$\begin{aligned} T_0 \;=\; & \frac{\sigma}{\nu^2}\left(\frac{3\sqrt{R^2+8R} - R - 8}{2}\right. \\ & +\; \log\frac{R^2+8R+8+(R+4)\sqrt{R^2+8R}}{8} \\ & +\; \left. R\log\frac{\sqrt{R^2+8R}-R}{8}\right). \end{aligned} \qquad (15)$$

There is, however, an important distinction between the Van der Pol equation and our situation: in the former case the fast system is one-dimensional, therefore relaxation to the respective slow curve is monotonic. In our case, the fast subspace is three-dimensional. On the side branches, all three roots of Eq. (12) are real only in the immediate vicinity of the extrema of the curve; elsewhere along the branches the characteristic polynomial has a pair of complex-conjugate roots. Moreover, the (negative) real part of those eigenvalues lies closer to zero than the single real eigenvalue, therefore relaxation to the side branch on the fast timescale is oscillatory. Except for this circumstance, the rest of the above description of relaxation oscillations remains qualitatively and quantitatively correct. An illustration is provided in Fig. 5 and Fig. 6 where time evolution of the variables as well as projections of phase portraits are presented.

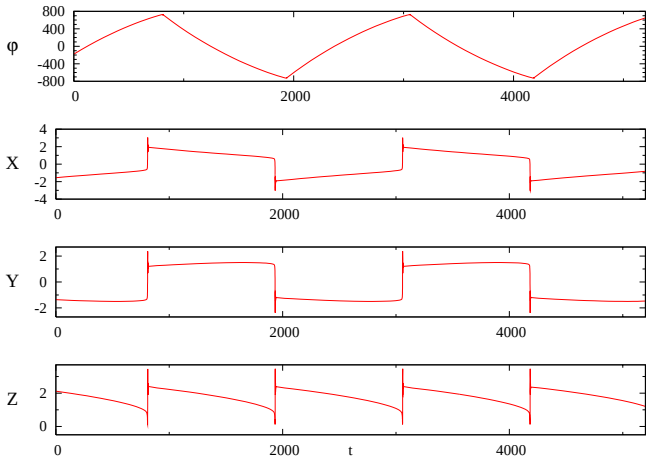

FIG. 5: (color online) Temporal evolution of variables. $\sigma = 10,\ R = 3,\ \nu = 0.1$.

Large "overshoots" which precede the segments with nearly constant slope in the time series of fast variables X, Y, Z in three lower panels of Fig. 5, correspond to the starting points of the non-monotonic relaxation; a magnification of time axis would resolve here the rapidly decaying oscillations. As seen on the central panel of Fig. 6, during the slow stage the values of Ψ and X follow closely the dependence (9).

As soon as the value of R exceeds the threshold (13), segments of the side branches adjacent to the extrema become unstable. Stability is restricted to the outer parts with

$$|X| > X_h = \left[\frac{\sigma\left(R - 8 - 2\sigma + \sqrt{(R-4-2\sigma)^2 + 8R}\right)}{4} - 1\right]^{1/2}. \qquad (16)$$

On reaching from outside the point with $X = X_h$, the equilibrium state in the fast subsystem gets destabilized

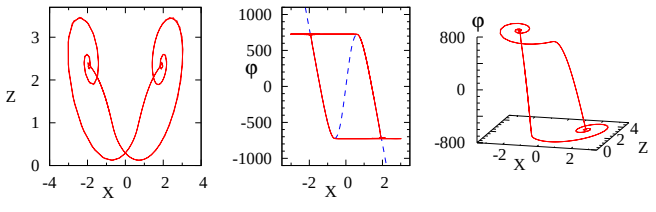

FIG. 6: (color online) Projections of phase portrait. $\sigma = 10$, $R = 3$, $\nu = 0.1$. Dashed line on the central panel: dependence (9).

via the subcritical Hopf bifurcation. Therefore not only the fast relaxation to the slow curve as before, but also the departure from it at $X \approx X_h$ becomes oscillatory. This is visible in the right and left panels of Fig. 7. Compared to Fig.6, additional tight wiggles appear on the phase portraits. The overwhelming portion of time, however, is spent not on the spirals but on the nearly straight "vertical" segments of the right panel. As seen in

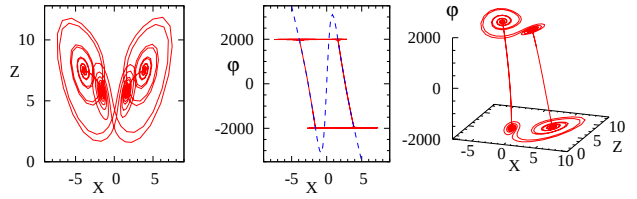

FIG. 7: (color online) Projections of phase portrait. $\sigma = 10$, $R = 8$, $\nu = 0.1$. Dashed line on the central panel: dependence (9).

the central panel of Fig.7, for $R > R_{\rm TB}$ the regions adjacent to extrema of $\Psi(X)$ are not visited by trajectories of the system. In this situation both the amplitude and the period of oscillations fail to reach the values predicted, respectively, by (17) and (15). Instead, the amplitude turns into

$$\Phi_1 = \frac{2\,\sigma\,X_h}{\nu^2}\left(1 - \frac{R}{1+X_h^2}\right) \qquad (17)$$

and the period, becomes

$$T_1 = \frac{2\,\sigma}{\nu^2}\left(\frac{R\,(X_{h1}^2 - X_h^2)}{(1+X_h^2)(1+X_{h1}^2)} + (R-1)\log\frac{X_h}{|X_{h1}|} - \frac{R}{2}\log\frac{1+X_h^2}{1+X_{h1}^2}\right), \qquad (18)$$

X_{h1} being the coordinate of the point on the slow curve to which the system relaxes after a jump from X_h:

$$X_{h1} = -\frac{RX_h + \sqrt{R^2X_h^2 - 4(1+X_h^2)(1+X_h^2-R)}}{2\,(1+X_h^2)}.$$

Dependencies (17) and (18) are non-monotonic functions of R. Segments of growth immediately beyond R_{TB} are succeeded by decrease of both characteristics. Finally, at $R{=}R_h{=}\sigma(\sigma{+}4)/(\sigma{-}2)$ the value of Ψ which corresponds to X_h and X_{h1} turns into zero, and the amplitude of relaxation oscillations vanishes. Obviously, the period vanishes at this value of R as well.

V. CORRECTIONS TO THE ESTIMATES: BIFURCATION DELAY

In the above estimates the actual period was replaced by the time interval during which the system creeps along the stable part of the slow curve; duration of motion outside the slow curve has been neglected. Asymptotically correct in the limit $\epsilon \to 0$, these estimates become less accurate at finite values of ϵ. Expressions (15) and (18) yield values of period which are proportional to ϵ^{-1}. Duration of the neglected epochs of flight is of the order of $O(1)$. However, main corrections to (15) and (18) stem not from these epochs.

The case of $R < R_{\rm TB}$ is straightforward: here, the system detaches from the slow curve near the extrema of the latter. This situation is very close to the well-studied case of the Van der Pol equation [12]: the leading order terms in the correction correspond to the time which the system spends hovering near the extremum of the slow curve, as well as to the "landing" time after the flight; this time (up to logarithmic corrections) is proportional to $\epsilon^{-1/3}$. According to Eq. (15), the passage time T_0 along the slow curve is proportional to ϵ^{-1}, therefore the overall period of oscillations can be cast into the form

$$T = T_0\,(1 + C\epsilon^{2/3} + \text{h.o.t.}) \qquad (19)$$

where the prefactor C is the function of the system parameters σ and R (an expression much too lengthy, to be quoted explicitly). This dependence is verified numerically in Fig. 8.

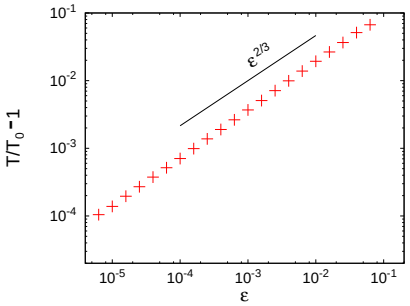

FIG. 8: (color online) Period of oscillations at $R < R_{\rm TB}$: Corrections to the estimate (15). $\sigma = 10$, $R = 2.5$. T_0 is given by Eq. (15). Crosses: numerical values.

The case $R > R_{\rm TB}$ is qualitatively different. Here, the imaging point might be expected to detach from the slow curve on reaching the value $\pm X_h$: there the curve becomes repelling due to the Hopf bifurcation in the fast system. For an exemplary case σ=10, illustrated in Fig.

9. the value of $R_{\rm TB}$ equals 2.91016...; beyond it, the estimates (17) and (18) for the amplitude and the period of oscillations, respectively, should hold.

Instead, we observe that approximately until R=4.5 the computed values stay rather close to the predictions (14) and (15). In this range of R the trajectory tracks the complete unstable segments of the slow curve, and detaches only near the extrema of the latter. For $R > 4.5$, as seen in the plots, the computed characteristics stay below the predictions of (14) and (15); at the same time, they remain distinctly above the estimates (17) and (18). Consequently, here the system follows the unstable segments as well, but leaves the vicinity of the slow curve before this curve turns back. Contribution of unstable segments increases the amplitude of the oscillations; duration of the passage along them contributes to the period.

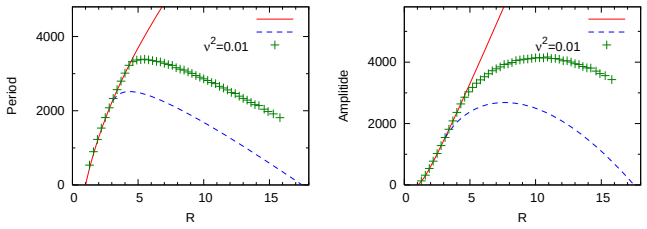

FIG. 9: (color online) Predicted and numerically observed characteristics of oscillations. $\sigma = 10$, $\nu = 0.1$. Solid lines: estimates (15) and (14). Dashed lines: estimates (18) and (17). Crosses: numerical values (integration with double precision).

This phenomenon is known as "bifurcation delay" or "dynamic bifurcation" [13, 14]. In the immediate vicinity of X_h the growth rate of the instability is arbitrarily small, whereas the velocity of motion *along* the slow curve is small but finite. Therefore for some time the system continues its motion along the unstable part of the slow curve; only later it departs and makes a jump to the opposite branch of this curve.

For a dynamical system with finite smoothness (or even infinitely smooth but non-analytic one), the length of the "added" part of the trajectory: segment of the slow curve between the point of the destabilization and the point of the jump, has an order of $\sqrt{\epsilon|\log\epsilon|}$ [15]. In practice, it is convenient to use the value $\sqrt{\epsilon}$. Since the velocity of motion along the curve is inversely proportional to ϵ, the gain in period is $\sim \epsilon^{-1/2}$. In natural or numerical experiments smoothness of the process is always finite, due to inevitable fluctuations in the former case and roundoff errors in the latter one. Accordingly, we can expect that the observed period follows the dependence $T \approx T_1(1 + C\epsilon^{1/2})$ where T_1 is given by the estimate (18). Indeed, the numerical experiments vindicate this conjecture. However (in contrast to the above case $R < R_{\rm TB}$), for the given set of parameters σ and R the value of the prefactor C is not unique. The prefactor depends on the limitations in the observations: on the level of noise in your setup, if you are an experimentalist, and, remarkably, on the length of the representation of real numbers in your computer if you are performing accurate numerical simulations.

This dependence is visualized in the top panels of Fig. 10. We performed integration of the equations under the same parameter values, with the same algorithm – recurrent Taylor expansion of high order with variable stepsize and the relative error per step at the level of the roundoff error – but took different representation of floating point numbers in the FORTRAN code: *ordinary* numbers with 7 decimals, *double precision* numbers with 16 decimals and *quadruple precision* numbers with 34 decimals[19]. As seen in the top left top panel, in all three cases the relative accuracy $(T - T_1)/T_1$ is proportional to $\sqrt{\epsilon}$, but the proportionality coefficients (top right panel) are distinctly different.

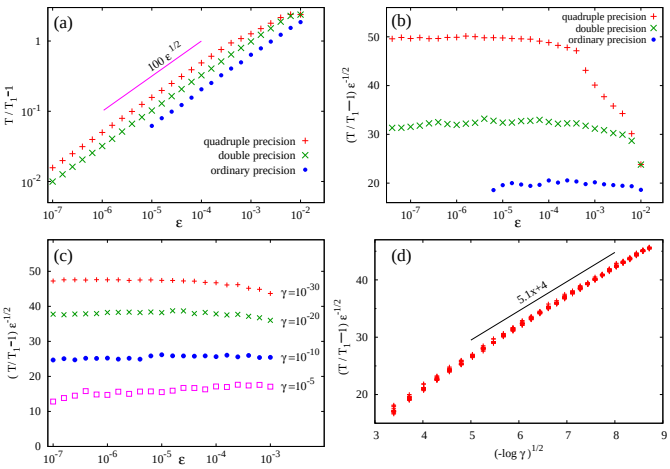

FIG. 10: (color online) Influence of the floating number length on bifurcation delay. Parameters: $\sigma = 10$, $R = 12$. T_1 is given by Eq. (18). Panels (a,b): deterministic computations; (c) computations with a random shift of trajectory after every step. Shift size was taken from a uniform distribution on the interval $(-\gamma/2, \gamma/2)$; (d) computations at $\nu = 0.1$ ($\epsilon = 0.001$). Dependence of slope on the uncertainty γ.

The length of the floating point representation can be understood as a measure of intrinsic numerical noise caused by roundoff errors: disturbances which keep the solution away from the "true" integral curve. Remarkably, only this length seems to matter: in contrast, integration of equation with different orders of the Taylor series expansion (in other words, different degrees of smoothness of approximate solution) does not seem to influence the prefactor.

Interrelation between the size of the roundoff error and the duration of the delay follows from the simplified qualitative analysis of the final stage of the slow motion. The question of interest is, how soon the trajectory reaches the given distance from the curve. Therefore torsional components of the motion in the phase space are of less importance, and two local coordinates suffice: the lon-

gitudinal ξ *along* the slow curve and the "transversal" ζ which measures the distance *from* that curve. Let the origin in this new coordinate system lie in the point on the slow curve with $X = X_h$. Close to X_h, the growth rate of ζ, given by the real part of the leading eigenvalues in the fast system, is proportional to $X - X_h = \xi$; velocity of motion along the slow curve is, in this approximation, constant. Accordingly, dynamics obeys the equations

$$\dot{\xi} = A_1\epsilon, \qquad \dot{\zeta} = A_2\xi\zeta \tag{20}$$

with appropriate positive constants $A_{1,2}$. Let the trajectory start at $\xi = 0$. A straightforward calculation shows that the time τ_d required for the growth of ζ from initial ζ_0 to the endpoint ζ_1 is given by

$$\tau_d^2 = \frac{2}{\epsilon\, A_1 A_2} \log\frac{\zeta_1}{\zeta_0}\,; \tag{21}$$

at the end of this time interval the coordinate ξ attains the value $\epsilon\,\tau_d$. For our purposes, the endpoint ζ_1 should correspond to the border of validity of Eqs. (20): as soon as this border is reached, the delay is over, the system leaves the neighborhood of the unstable branch of the slow curve and begins its fast flight to the opposite branch. As for the starting value ζ_0, it is a measure of decline from the slow curve at X_h. Since passage through X_h is preceded by the long epoch of motion along the attracting segment of this curve, the transients must have decayed and can be viewed as negligibly small. Therefore the mismatch ζ_0 is of the size of the error produced by the very last step of numerical integration. Denoting by γ the length of uncertainty interval introduced by the last roundoff error, we set $\zeta_0 \approx \gamma$, whereupon expression (21) yields for the delay time τ_d and the "delay path" p_d (increment to the amplitude of the oscillations) qualitative dependencies

$$\tau_d \sim \sqrt{-\frac{\log\gamma}{\epsilon}}, \qquad p_d \sim \sqrt{-\epsilon\log\gamma}. \tag{22}$$

A roundoff error can be (modulo implementation particularities for different compilers) viewed as a random shift in the last meaningful digit. In order to model this effect for the lengths of representation which are not directly available to the FORTRAN code, we performed computations in which, after every step, all four coordinates of the point in the phase space were randomly shifted; sizes of shifts were taken from the homogeneous distribution on the interval $(-\gamma/2, \gamma/2)$. Results are presented in the bottom panels of Fig. 10. On the bottom left panel we observe the same square-root scaling in the dependence on ϵ. On the bottom right panel, the value of ϵ is fixed, and linear dependence between the values of prefactors and $\sqrt{-\log\gamma}$ is doubtless. Keeping this in mind, we rewrite the above expression for the overall period as

$$T \approx T_1\left(1 + C_1(-\epsilon\log\gamma)^{1/2}\right) \tag{23}$$

where the uncertainties of computation are explicitly represented through the value of γ, and the constant C_1 depends only the parameters of the problem R and σ.

Finally, we checked the influence of noise on the bifurcation delay by adding the term $\sqrt{2D}\xi(t)$ to the right hand size of the equation of motion; here, D is the intensity of the delta-correlated Gaussian white noise $\xi(t)$ with unit variance. Results are plotted in Fig. 11 and are largely similar to the above cases of roundoff errors: relative increase of period is proportional to $\epsilon^{1/2}$. Rigorous analysis for the delay of pitchfork bifurcation in case of additive noise, performed in [16], predicts the typical delay path of the order of $\sqrt{\epsilon|\log D|}$.

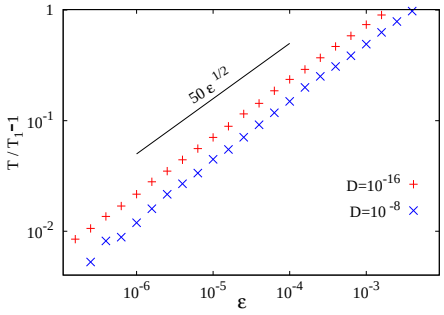

FIG. 11: (color online) Influence of noise on the increase of the oscillation period. Langevin simulations with additive Gaussian white noise of intensity D. Parameters: $\sigma = 10$, $R = 12$. T_1 is given by Eq.(18).

Notably, the validity of (23) requires that intensity of additive or numerically caused noise is small compared to ϵ (more precisely, the rate of noise-induced fluctuations of coordinates should be smaller than the deterministic velocity of slow drift). As soon as this condition becomes violated, noise enables early departures from the slow curve, and the scaling law breaks down. For this reason, in the plots of Fig. 10c and Fig. 11 the left segments of the respective lowest curves display visible deviations from the general dependence.

As a result of bifurcation delay, the *computed* relaxation oscillations are not strictly periodic. Numerical trajectories are discrete, and the "next to X_h" points on subsequent turns of the orbit do not coincide. Hence, the moment when the initial fluctuation is introduced varies slightly, and the whole duration of the delay varies as well within 1-2% of its mean value. Therefore, the segments of flight between the branches of the slow curve fail to repeat each other. This effect is visible e.g. in the double spirals of Fig. 7, as well as in the slight scattering of numerical values of periods in the bottom right panel of Fig. 10. Due to this effect, the numerically observed state is only approximately periodic. However, one cannot speak about chaos: long intervals of contraction near the stable segments of the slow curve dominate in the computation of averaged quantities, therefore all Lyapunov exponents are negative.

VI. COLLAPSE OF THE RELAXATION OSCILLATIONS

With the further growth of R, the value of X_h moves away from the minimum of the slow curve, and the segments of that curve which participate in the oscillatory process become ever shorter. At the first sight, this process might go on until $R_h = \sigma(\sigma+4)/(\sigma-2)$ when the value of Ψ corresponding to X_h and X_{h1} vanishes, and the "working interval" of the slow curve shrinks completely. In fact, the regime of relaxation oscillations breaks down earlier. This owes to the subcritical character of the Hopf bifurcation which occurs at X_h in the fast equations. The unstable periodic orbit, born in this bifurcation, encircles the stable equilibrium on the slow curve and restricts its local basin of attraction. This periodic orbit of fast equations exists in an interval of values of Ψ; on the opposite border of the interval, it disappears in the homoclinic bifurcation of the saddle "equilibrium" from the central part of the slow curve.

In an asymmetric variant of the Lorenz equations, there is no "homoclinic explosion"[11] which would instantaneously create in the phase state an infinite set of unstable periodic orbits and aperiodic trajectories. Instead, this set is created by the sequence of secondary homoclinic bifurcations. Here we do not aim at the complete description of the bifurcation scenario; it suffices to state that the newborn set is not attracting. However, as the slow variable Ψ moves in the direction of the Hopf bifurcation, the chaotic state can get stabilized. As a result, there exists a range of R values in which the stable equilibria upon the slow curve are not the only attractors of the fast system: they coexist with the attracting chaotic set akin to the Lorenz attractor. The stable manifold of the described unstable periodic orbit separates the attraction basin of the equilibrium from the attraction basin of the chaotic set. As long as the trajectory of the fast system which leaves the slow curve near X_h, jumps straight into the attraction basin of the equilibrium at X_{h1}, dynamics remains similar to that of Fig. 7. However, as soon as this jump ends up on the opposite side of the separatrix, the fast subsystem evolves into the chaotic state and never reaches the slow curve again. This event marks the end of the regime of relaxation oscillations.

Bifurcation delay plays a certain quantitative role in this transition as well: it effectively enlarges the working intervals of the slow curve, adding to them the nearby parts of the unstable segments. Transition from relaxation oscillations to chaos is illustrated in Fig. 12. The calculations were made at $\sigma = 10$ and $\nu = 0.1$. Collapse of relaxation oscillations was registered at $R = 17.1354$ (for comparison, $R_h = 17.5$, whereas the chaotic set in the phase space becomes attracting at $R = 15.328$). Obviously, the geometry of attractors for $R = 17.135$ and $R = 17.136$ is qualitatively very much different. This concerns not only the angular variable φ, but the "Lorenz" variables X, Y and Z as well. In terms of those

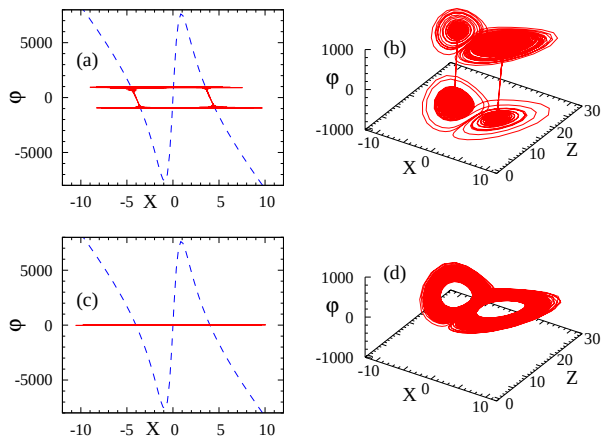

FIG. 12: (color online) Projections of phase portraits. $\sigma = 10$, $\nu = 0.1$. (a,b): $R = 17.135$; (c,d): $R = 17.136$. Dashed lines on (a) and (c): dependence (9).

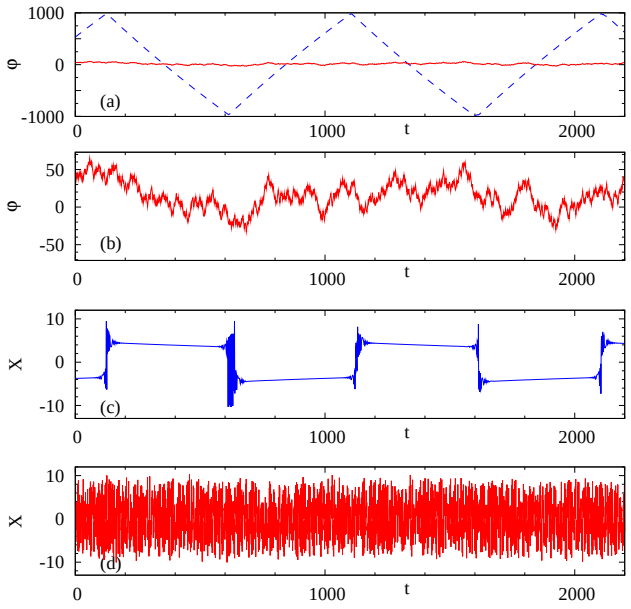

FIG. 13: (color online) Temporal evolution of variables before and after the breakup of relaxation oscillations. Parameter values: $\sigma = 10$, $\nu = 0.1$. (a) Dashed and solid lines: $\varphi(t)$ at $R = 17.135$ and $R = 17.136$, respectively. (b) Temporal pattern of $\varphi(t)$ at $R = 17.136$. (c,d): $X(t)$ at $R = 17.135$ and $R = 17.136$, respectively.

variables, before the transition the attractor consisted of regular segments of spirals separated by quasistationary translations. After the transition, spirals get replaced by the pattern, typical for the Lorenz-like attractors. In the course of chaotic motion, the fast variable X oscillates erratically between positive and negative values, the long-time average $\langle X \rangle$ stays relatively small and (on the slow timescale) occasionally changes the sign. This, in its turn, prohibits the large-scale variation of φ, so that the chaotic attractor turns out to be strongly compressed

along φ; the amplitude of torsional oscillations of the pendulum falls severely.

Typical examples of temporal evolution of the angle before and after the breakdown of relaxation oscillations are presented in Fig. 13a,b. As seen in the upper panel, after the transition the variation range of the angle φ contracts by more than an order of magnitude. Fine structure of the dependence $\varphi(t)$ is shown in Fig. 13b where the random-walk character of the behavior makes a sharp contrast to the previously described long segments of monotonic evolution. For the Lorenz variables, the transition is nonetheless drastic, but in a sort of different way. According to two lower panels of Fig. 13, the amplitude of variation for those variables does not change especially; what changes, is the character of the dynamics: Long segments of quasistationary evolution and short "spiralling" intervals disappear, yielding to irregular rotations.

In the chaotic state, the variable Ψ is not slow anymore; separation of timescales becomes invalid. Detailed investigation of chaotic solutions for the Quincke pendulum lies outside the scope of the current paper and will be described elsewhere. Here we just mention one of the noteworthy effects. In a certain region of parameter values, the chaotic attractor exhibits a symmetry-breaking; two new attractors appear, for which either of the torsional directions (clockwise or counterclockwise) is preferred. From the point of view of nonlinear dynamics this is a well-studied phenomenon; from the point of view of an experimentalist, this would mean a surprising observation: the Quinke pendulum performs erratic small-amplitude oscillations not around its mechanical equilibrium, but around certain particular non-zero values of the torsional angle.

Acknowledgement

M.Z. acknowledges the support of DFG Research Center Matheon "Mathematics for Key Technologies".

[1] G. Quincke, Ann. Phys. Chem. **59**, 418 (1896).
[2] A. O. Tsebers, Izv. Akad. Nauk SSR, Mekh. Zhidk. i Gaza, No.2, 86 (1980) [in Russian].
[3] T. B. Jones, IEEE Trans. on Industry Appl. **IA-20**, 845 (1984).
[4] L. Lobry and E. Lemaire, J. Electrostatics **47**, 61 (1999).
[5] N. Pannacci, L. Lobry, and E. Lemaire, Phys. Rev. Lett. **99**, 094503 (2007).
[6] E. Lemaire and L. Lobry, Physica A **314**, 663 (2002).
[7] L. D. Landau and E. M. Lifshitz, *Fluid Mechanics* (Nauka, Moscow, 1986).
[8] F. Peters, L. Lobry, and E. Lemaire, Chaos **15**, 013102 (2005).
[9] A. Cebers, E. Lemaire, and L. Lobry, Magnetohydrodynamics **36**, 347 (2000).
[10] E. N. Lorenz, J. Atmos. Sci. **20**, 130 (1963).
[11] C. Sparrow, *The Lorenz equations : Bifurcations, chaos, and strange attractors* (Springer, 1982).
[12] A. A. Dorodnitsin, Prikl. Mat. Mekh. **11**, 313 (1947) (in Russian).
[13] V. I. Arnold (Editor), *Dynamical Systems V: Bifurcation Theory and Catastrophe Theory. Encyclopaedia of Mathematical Sciences* (Springer, New York, Berlin, 1999).
[14] *Dynamic Bifurcations*, Lect. Notes Math. **1493**, edited by E. Benoît (Springer-Verlag, 1991).
[15] A. I. Neishtadt, Uspekhi Mat. Nauk **40**, 300 (1985).
[16] N. Berglund and B. Gentz, Probab. Theory Relat. Fields **122**, 341 (2002).
[17] Strictly speaking, the last equation of the Lorenz system reads $\dot{Z} = XY - bZ$. Equations (4) at $\nu = 0$ correspond to the case b=1 which is largely similar to the well-studied original case $b = 8/3$.
[18] Within this description, the onset of oscillations occurs not at R_c but already at $R = 1$. Recall that ϵ is small, and $R_c = 1 + O(\epsilon)$.
[19] More accurately: 23, 52 and 112 binary digits, respectively.